Tectonophysics 848 (2023) 229730

Contents lists available at ScienceDirect

Tectonophysics

journal homepage: www.elsevier.com/locate/tecto

Bouguer gravity anomalies and the three-dimensional density structure of a thick mudstone area: A case study of southwestern Taiwan

Yu-Tsung Lo [a], Kuo-En Ching [b], Horng-Yuan Yen [a,*], Song-Chuen Chen [c]

[a] Department of Earth Sciences, National Central University, Taiwan
[b] Department of Geomatics, National Cheng Kung University, Tainan, Taiwan
[c] Central Geological Survey, Ministry of Economic Affairs, Taiwan

ARTICLE INFO

Keywords:
Gravity inversion
Southwestern Taiwan
Residual gravity
Mud-diapir

ABSTRACT

Gravity surveying is one of the best methods to deduce the subsurface structures in areas covered by thick mudstone in southwestern Taiwan where seismic data analysis is limited. We obtained regional and residual gravity anomalies from the Bouguer anomaly map using the wavelength filtering method to image the gravitational effects of subsurface sources at different depths. The distribution of the residual gravity anomalies corresponds well with the locations of faults and anticlines. Through the change of residual gravity anomalies due to sources at different depth, we estimated the inclination and extension of the anomalous bodies at different depths. Then, the three-dimensional density structure was inferred from inversion of the gravity data to reveal the distribution of mud diapirs and changes of depth to the basement. The positive residual gravity anomalies of approximately 1–2 mGal indicate that the material density of the diapirs is 0.1–0.2 g/cm^3 higher than the surrounding rock. The origin of positive residual gravity anomalies can be roughly divided into three types corresponding to the possible subsurface structures. The depth of the positive gravity anomaly below the major anticlines is approximately 4–5 km, corresponding to the bottom of the mudstone formation, from which the mud diapirs may originate. The residual gravity anomaly pattern also indicates a connection of the Chegualin and Youchang faults and the nearly vertical Zuochen fault above 10 km depth. Finally, the low gravity in the Pingtung Plain results from the high-density contrasts on both sides of the two major faults and the deepening of the basement in the plain. The high-angle Chauchou fault, one of two major faults, was also identified at shallow depths based on analysis of the gravity data.

1. Introduction

Southwestern Taiwan (Fig. 1), belonging to part of Taiwan's fold-and-thrust belt and the incipient collision stage between Eurasian and Philippine Sea plates (Shyu et al., 2005), is mainly underlain by thick mudstone (Chang et al., 1982). In addition, the high contraction rate of approximately 1.0 μstrain/yr detected by GNSS observations across SW Taiwan (Yu et al., 1997; Ching et al., 2007, 2011a) indicates that the development of faults and folds are currently active in the incipient collision stage. However, the active fault-dominated (Brown et al., 2022; Le Béon et al., 2017) and mudstone intrusion-dominated deformations (Hsieh, 1970; Chen et al., 2020; Rau et al., 2022) are two main schools to interpret the rapid contraction of thick mudstone across SW Taiwan. In other words, the ongoing active anticlines in SW Taiwan revealed by leveling and InSAR data, e.g., Tainan anticline (TNA) and Chungchou anticline (CCA), could be contemporary explained as the fault-related folds or mud diapirs. The debate of cause of the fold structure is not only related to the mechanism of mountain building, but also related to the seismic hazard assessment in the incipient collision of Taiwan.

The geological data including outcrops in SW Taiwan is limited to distinguish the cause of the fold structure so far. Considering the geophysical results, a relatively low seismic wave velocity in the crust in this area appears in the seismic tomography models (Kuo-Chen et al., 2012; Huang et al., 2014). However, almost no earthquakes have occurred at depths shallower than 15 km, and seismic tomography has limited analytical capabilities for depths shallower than 5 km as can be seen in the seismic data for SW Taiwan (Kuo-Chen et al., 2012; Huang et al., 2014). The seismic reflection method is one of the effective methods used to determine the undulations and depths of strata to construct the structural cross-sections. However, it is difficult to obtain

* Corresponding author at: Department of Earth Sciences, National Central University, Chung-Li, Taiwan, ROC.
E-mail address: yenhy@cc.ncu.edu.tw (H.-Y. Yen).

https://doi.org/10.1016/j.tecto.2023.229730
Received 19 July 2022; Received in revised form 16 January 2023; Accepted 20 January 2023
Available online 24 January 2023

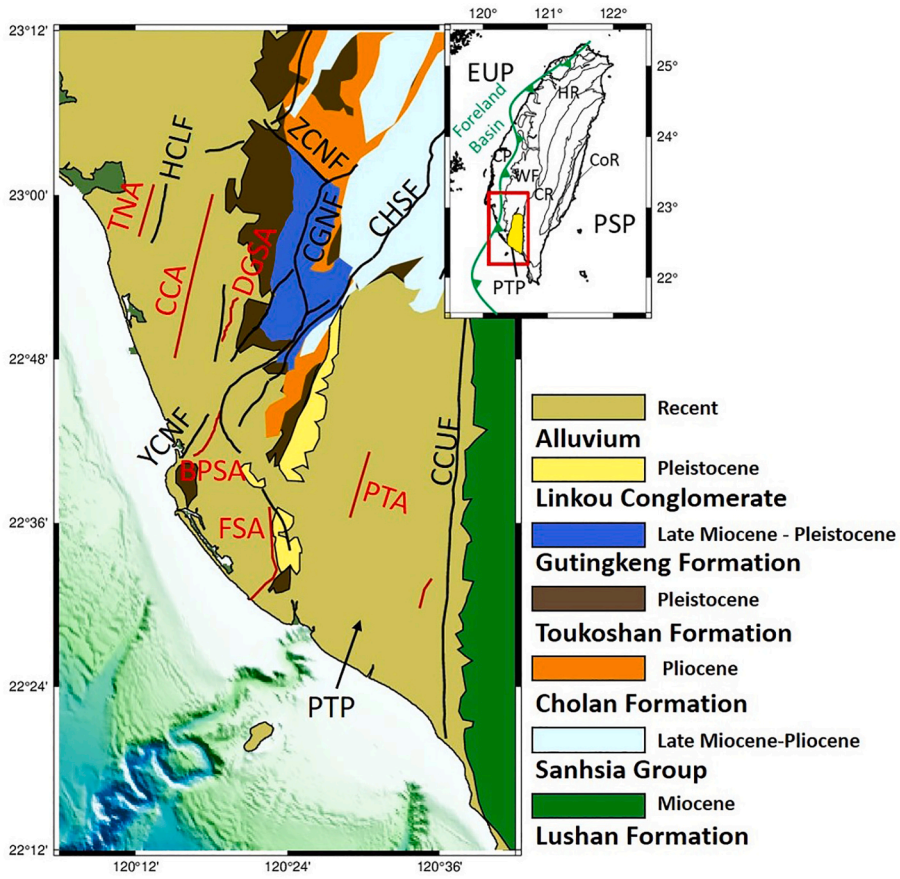

Fig. 1. Regional geological map of southwestern Taiwan, modified from the geological map of the Central Geological Survey, MOEA. (CP: Coastal Plain; WF: Western Foothills; HR: Hsuehshan Range; CR: Central Range; CoR: Coastal Range; PSP: Philippine Sea Plate; EUP: Eurasian Plate; HCLF: Houchiali fault; ZCNF: Zuochen fault; CGNF: Chequalin fault; CHSF: Chishan fault; YCNF: Youchang fault; CCUF: Chauchou fault; TNA: Tainan anticline; CCA: Chungchou anticline; DGSA: Dagangshan anticline; BPSA: Banpingshan anticline; FSA: Fengshan anticline; PTA: Pingtung anticline; PTP: Pingtung Plain.

good-quality seismic data in the coastal plain in SW Taiwan because of the thick mudstone (Huang et al., 2004). Although the gravity method has the limitation of a non-unique solution, the gravity survey is one of the optimal methods for identifying lateral variations of an extensive shallow structure with no overturning or overlapping old strata existing in a sedimentary environment under the constraints of geological and other geophysical data.

Since the gravity method has a good ability to identify structures in shallow layers, we are committed to obtaining a shallow gravity anomaly distribution and density model to discuss with other shallow models. We therefore first compiled the gravity data to evaluate the gravity anomalies in the area. The wavelength filtering method and three-dimensional gravity inversion constrained by geological data were used to explore the spatial variations of the gravity anomalies and subsurface density structure. The morphologies of shallow active structures in the mudstone-rich region and the proposed piggy-back basin, the Pingtung Plain, were then determined to better understand the tectonics, crustal deformation, and disaster prevention in this area.

2. Geological background

The Taiwan orogen is evolving as a result of the convergence between the Luzon Arc located on the Philippine Sea Plate and the continental margin of the Eurasian Plate since the latest Miocene (Fig. 1; Ho, 1986; Suppe, 1981). From west to east, the Taiwan orogen has been divided into five roughly N-S-oriented tectonostratigraphic zones (Fig. 1): the Coastal Plain (CP), the Western Foothills (WF), the Hsuehshan Range (HR), the Central Range (CR), and the Coastal Range (CoR). The WF in SW Taiwan are then composed of a series of basement-involved imbricated fold and thrust sheets (Mouthereau et al., 2002). The basement which is synrift and postrift margin sequences of the Late Miocene are loaded by the sediments which make up the foreland basin in SW Taiwan. The SW Taiwan has belonged to a part of the foreland basin that undergoes lithospheric flexuring attributed to the tectonic loading of the Central Range since the Pliocene (Teng, 1987; Lin and Watts, 2002). The depth of the foreland basin in this region may be up to 9 km, based on the presence of an obvious Bouguer gravity low over the area (Yen and Hsieh, 2010), the inferred magnetic basement surface (Yu and Tsai, 1981), and the foreland basin sequence (Lin and Watts, 2002).

In SW Taiwan, two geological domains are divided by the Chishan fault (CHSF). To the west of the CHSF, Pliocene to Pleistocene Gutingkeng formation (Gtk) mainly lies in the study area and forms a well-exposed badland topography. The thickness of Gtk is 3–4 km. The distribution range of Gtk is from the south of Chukou to Yanchao, presenting a long and narrow distribution in SW Taiwan. The Lower Gtk consists of gray siltstone or mudstone intercalated with lenticular graywacke and subgraywacke, while the Upper Gtk consists of gray sandy siltstone and sandy mudstone intercalated with lenticular graywacke and subgraywacke with abundant mollusca (Chou, 1971).

In the east of the CHSF, the Pingtung Plain (PTP) area of SW Taiwan is located in the transition between collision and subduction. The PTP area is characterized by a relative structural continuity and a homogeneous N—S trend, from the Taiwan collision belt in the north to the Manila Trench system in the south (Chang et al., 2002; Chang et al., 2009). The PTP is filled by the unconsolidated coastal and estuarine sediments of the late Pleistocene and the Holocene. The Linkou Conglomerate unconformably underlying the recent alluvium is a loose deposit. It is composed chiefly of gravels and pebbles of quartzose sandstone and intercalated with a thin layer of red clay in the middle part (Chiang, 1971). The conglomerate mainly comes from the rapidly uplifted CR. The Chaochou fault (CCUF) is another major fault in this domain, separating the PTP to the west and the hard shale, slate and phyllite of Lushan Formation comprising the CR to the east.

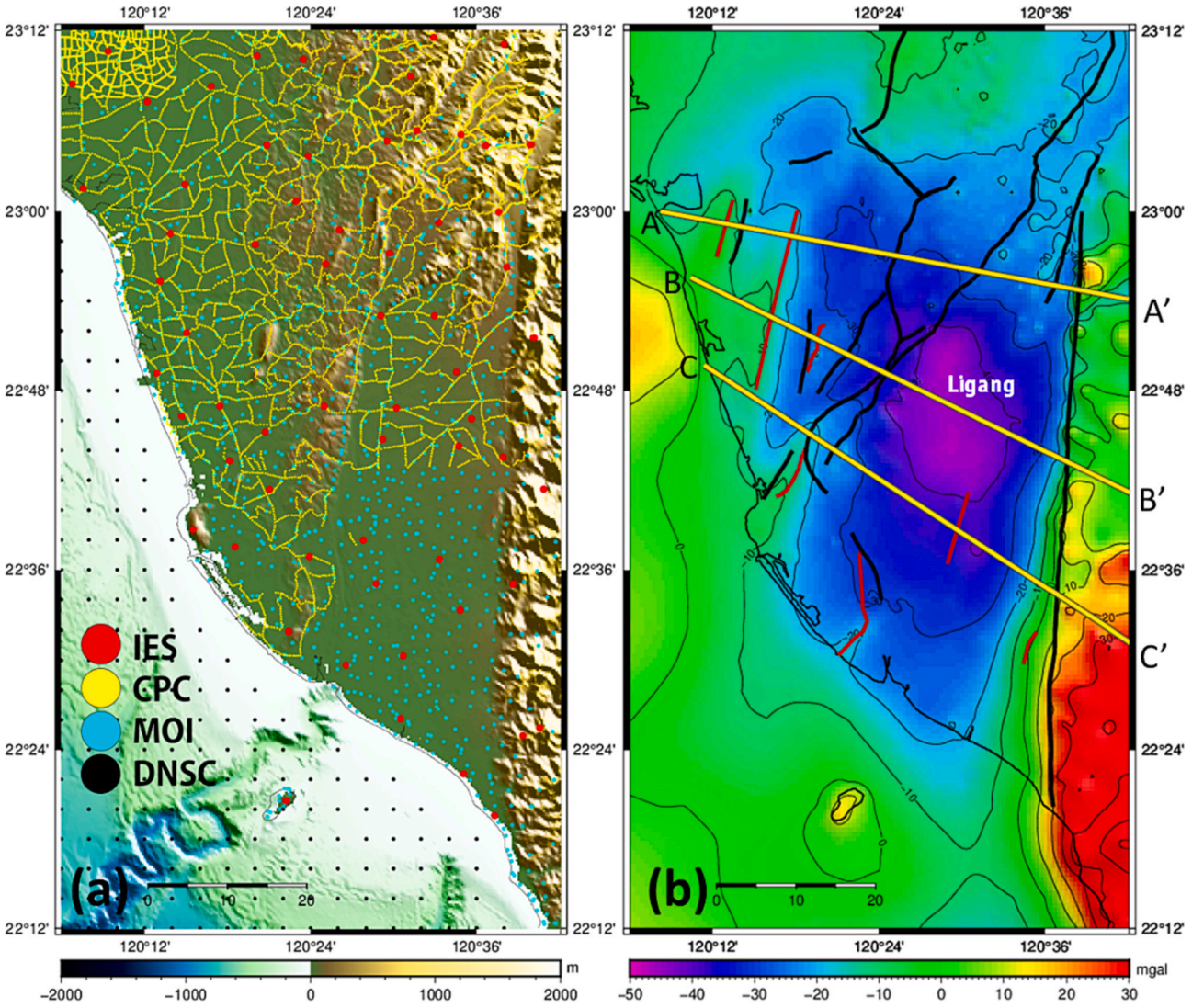

Fig. 2. (a) Distribution map of gravity measurement points and (b) Bouguer anomaly map of the study area. Gravity stations: IES, Institute of Earth Sciences, Academia Sinica; CPC, Chinese Petroleum Corporation; MOI, Ministry of the Interior; DNSC, Danish National Space Center.

3. Data and Method

3.1. Gravity data and Bouguer anomaly map

To obtain further insight into the detailed structure of SW Taiwan, we obtain residual gravity maps and carry out forward and inverse modeling of a high-resolution gravity data set. The gravity data were compiled from four sources (Fig. 2a): (1) 603 island-wide gravity stations that were installed by the Institute of Earth Sciences, Academia Sinica in 1980 (Yen et al., 1995), (2) 934 gravity stations that were selected from the Ministry of the Interior (MOI), (3) 9842 highly dense gravity data from the Chinese Petroleum Corporation (CPC) that had a site spacing of 200 m to 500 m and were mainly used for analyzing the detailed shallow structures in the study area, and (4) 176 satellite gravity data from Danish National Space Center (DNSC) was used to fill in offshore gravity data gaps with grid interval 1/3°.

We closely followed the data processing methodology of Yen and Hsieh (2010) to construct a Bouguer anomaly map (Fig. 2b) after applying latitude, free-air, Bouguer, and terrain corrections. Bouguer and terrain corrections were carried out with an average density of 2.57 g/cm^3 (Yen and Hsieh, 2010). The Bouguer anomaly ranged from −50 mGal to −10 mGal with the lowest values in the center of the PTP. The Bouguer gravity anomaly increases from the center to the outside with a high gravity gradient of about 3.5 mGal/km detected on the east side of the PTP, which mainly corresponds to the location of the high-angle CCUF. In addition, the study area is dominated by a broad gravitational low interspersed with several elongated gravitational highs along the coast. Determining the distribution and depth extent of the bodies causing the positive gravity anomalies is important for delineating the shallow geological structure of this area.

3.2. Wavelength filtering method

The Bouguer anomaly is the depth-integrated gravitational attraction of the subsurface density structure. The location of the source of the anomaly can be identified through the relationship between the wavelength of the anomaly and the source depth (Jung, 1961). A short-wavelength anomaly is dominated by a shallow density structure, whereas a deep structure generates a long-wavelength anomaly (Fig. 3a).

To investigate the depths of origin of the first-order regional gravity anomaly patterns, the wavelength filtering method (Jung, 1961) was applied to identify the general trends at various cut-off wavelengths (which are approximately associated with different depth ranges). The source depths of the anomalies were estimated using the 3-D approximate relationship between the maximum depth of a causative body (Z_s)

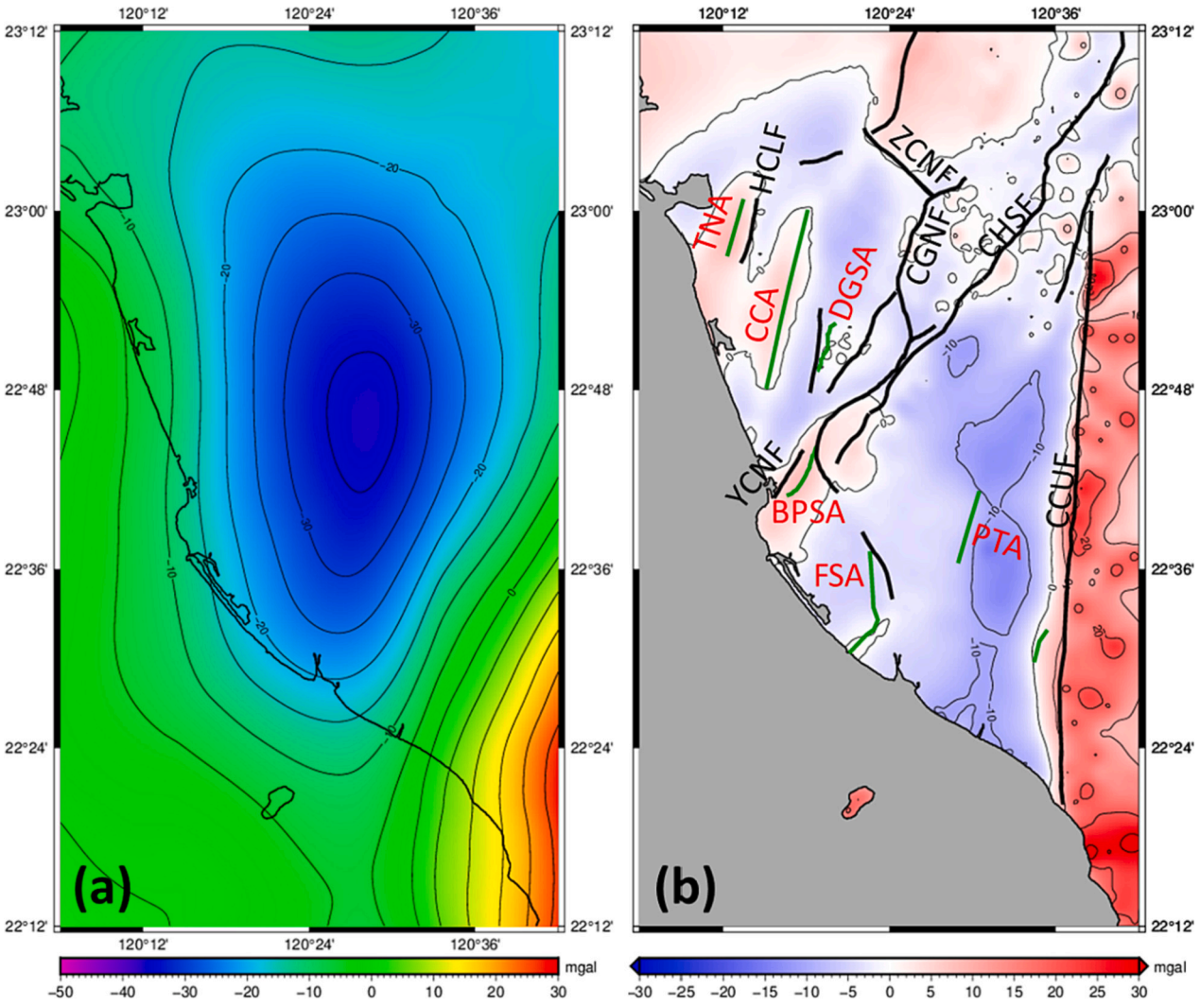

Fig. 3. Regional and residual gravity anomalies map. (a) Regional anomaly map obtained from the Bouguer map by applying a low pass filter (and reflecting density contrasts below 10 km); (b) residual anomaly map, the difference between the Bouguer and regional maps (reflecting density contrasts at shallower depths (0–10 km)).

and a certain cut-off wavelength (λ_c) given by Jung (1961) as:

$$\lambda_c \geq 3Z_s \tag{1}$$

From this relationship, it is possible to estimate the gravitational effects due to rocks at different depth ranges using different cut-off wavelengths. To examine the reliability of this concept, we establish two anomalous bodies that slope vertically and rightward to a depth of 5 km, forward their gravitational effect, and then conduct an analytical test of the wavelength filtering method. After that, the depth of the anomalous body and its gravity change can be determined (Fig. 4a and b). Although there is an anomalous value below 5 km depth, no obvious lateral anomalous value change is revealed. Therefore, this method is reliable if the anomalous body does not exist below 5 km depth.

To estimate the gravity effect due to different depth ranges, the Bouguer anomaly map was processed to obtain a regional map and a residual gravity anomaly map using different values of λ_c for filtering by Eq. (1). A long-wavelength regional anomaly map was first obtained by applying a low pass filter. The residual gravity anomaly map (short-wavelength anomalies) was derived from the original Bouguer map by subtracting the regional anomalies (Fig. 3b), and mainly reflects the lateral density changes of shallow structures, such as faults and folds. According to the residual gravity anomalies (representing source depths from 0 km to 10 km) (Fig. 3b)), the area is generally characterized by negative anomalies, and localized positive anomalies are mainly distributed along anticlines or the hanging walls of faults.

3.3. 3D forward calculation and density inversion method

The procedure for determining the three-dimensional forward and inversion models was based on that of Hsieh and Yen (2016). After establishing the subsurface density grid, the forward density model was first calculated. The gravitational attraction (g_{ij}) at the i^{th} gravity station from a certain point in the density grid j can be represented as:

$$g_{ij} = \rho_j G\left[\frac{Z_j dxdydz}{R_{ij}^3}\right] \tag{2}$$

where ρ_j is the density contrast of a density grid point j, G is the gravitational constant, Z_j is the depth of grid point j, and R_{ij} is the distance between the gravity station i, and grid point j. The forward gravity anomaly (g_i) created by the initial density model at the i^{th} gravity station is:

$$g_i = \sum_{j=1}^{n} g_{ij} = \sum_{j=1}^{n} \rho_j G\left[\frac{Z_j dxdydz}{R_{ij}^3}\right] \tag{3}$$

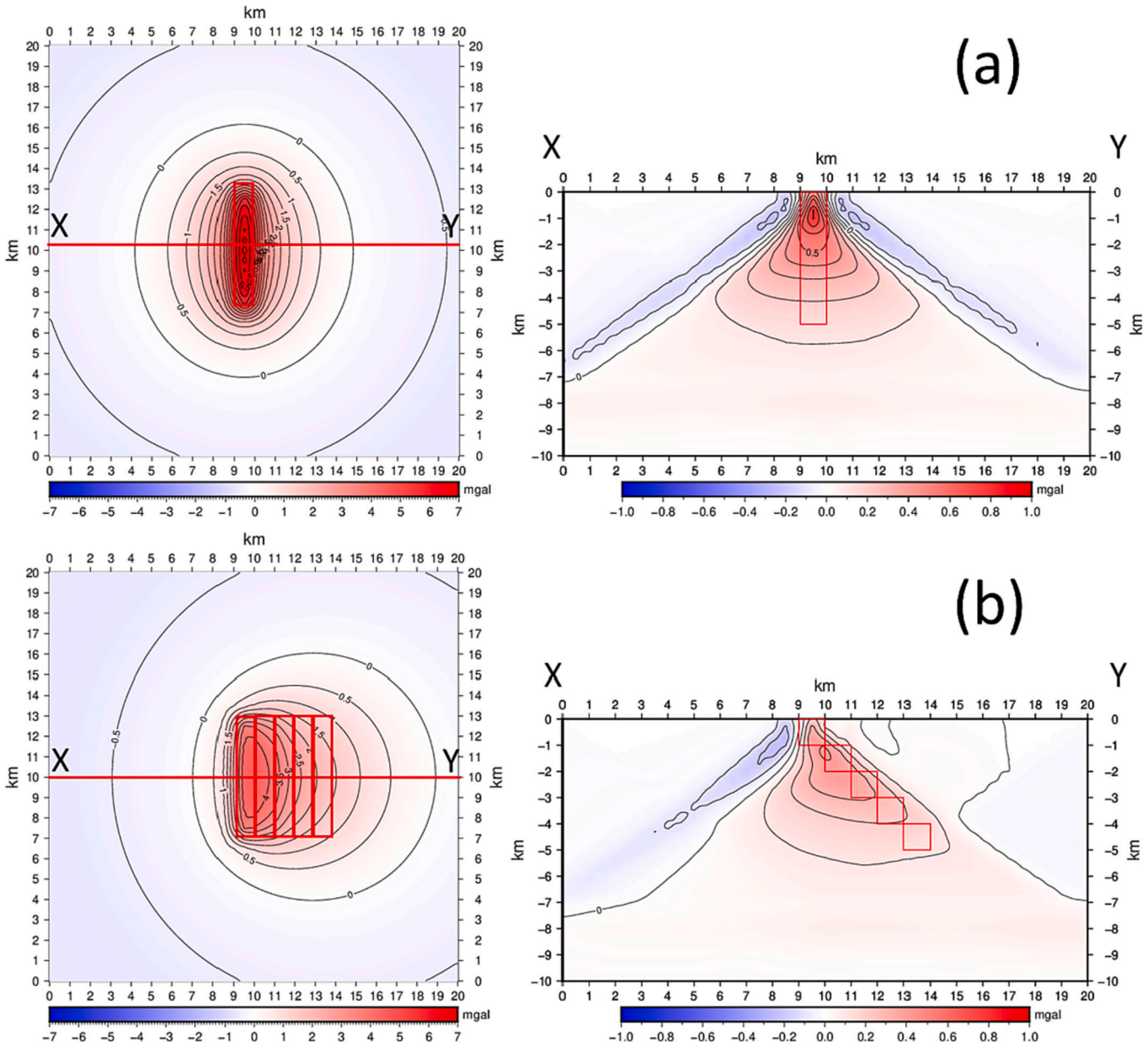

Fig. 4. A relatively high-density anomalous volume of 1x1x5 km was built to test the resolution of the wavelength filtering method. A relatively high-density anomalous body of 1x1x5 km was established to test the resolution of the wavelength filtering method (a) left: the calculated gravity value of the vertically upward anomalous body; right: the gravity variation with depth after wavelength filtering (b) left: Calculated gravity value of anomalous body tilted to the right; right: the gravity variation with depth after wavelength filtering.

where n is the total number of grids points. Then, the Bouguer anomaly distributions can be obtained by the summation of the gravitational attraction at each grid point g_{ij}.

The inversion modeling uses the least squares method to minimize the difference between the observed and theoretical gravity. The gravity anomaly g can be rewritten as:

$$g = A^{*}m \tag{4}$$

where A is the data kernel and m is the matrix of the model parameters. For the forward anomaly, g^{cal} can be scripted as:

$$g^{cal} = A^{*}m_i \tag{5}$$

where m_i is the initial matrix of model parameters. The observed Bouguer anomaly, g^{obs}, is:

$$g^{obs} = A^{*}m \tag{6}$$

where m is the matrix of a priori density model parameters. By comparing g^{cal} and g^{obs}, we obtained the difference, Δg, of the observed and calculated gravity anomalies:

$$\Delta g = g^{obs} - g^{cal} = \sum_{j=1}^{n} A^{*}\Delta m_j \tag{7}$$

The parameter Δg is the sum of the gravity effects from the density variation, Δm, of all grid points in the initial model. We used the least squares procedure to estimate the optimized grid densities in the study area. The error E is the residual between the previous difference, Δg, and the current difference after the density adjustment:

Table 1
Density of strata in southwestern Taiwan (Hsieh, 1970).

Geologic time	Stratigraphy	Density (g/cm^3)
Holocene	Recent Alluvium	1.9
Pleistocene	Lingkou Conglomerate	2.0
Pliocene	Gutingkeng Formation	2.2
Late Miocene	Basement	2.4–2.5
Miocene	Lushan Formation	2.55

$$E = \left\| \Delta g - \sum_{j=1}^{n} A^{*} \Delta m_j \right\|^2 \tag{8}$$

The error E is minimized by the least-squares method in an iterative process, and the optimal model is obtained when the error E is smaller than a pre-defined threshold value.

The final optimal density model (m_{final}) is obtained by summing the initial model (m_i) and the density variation value (Δm).

$$m_{final} = m_i + \Delta m \tag{9}$$

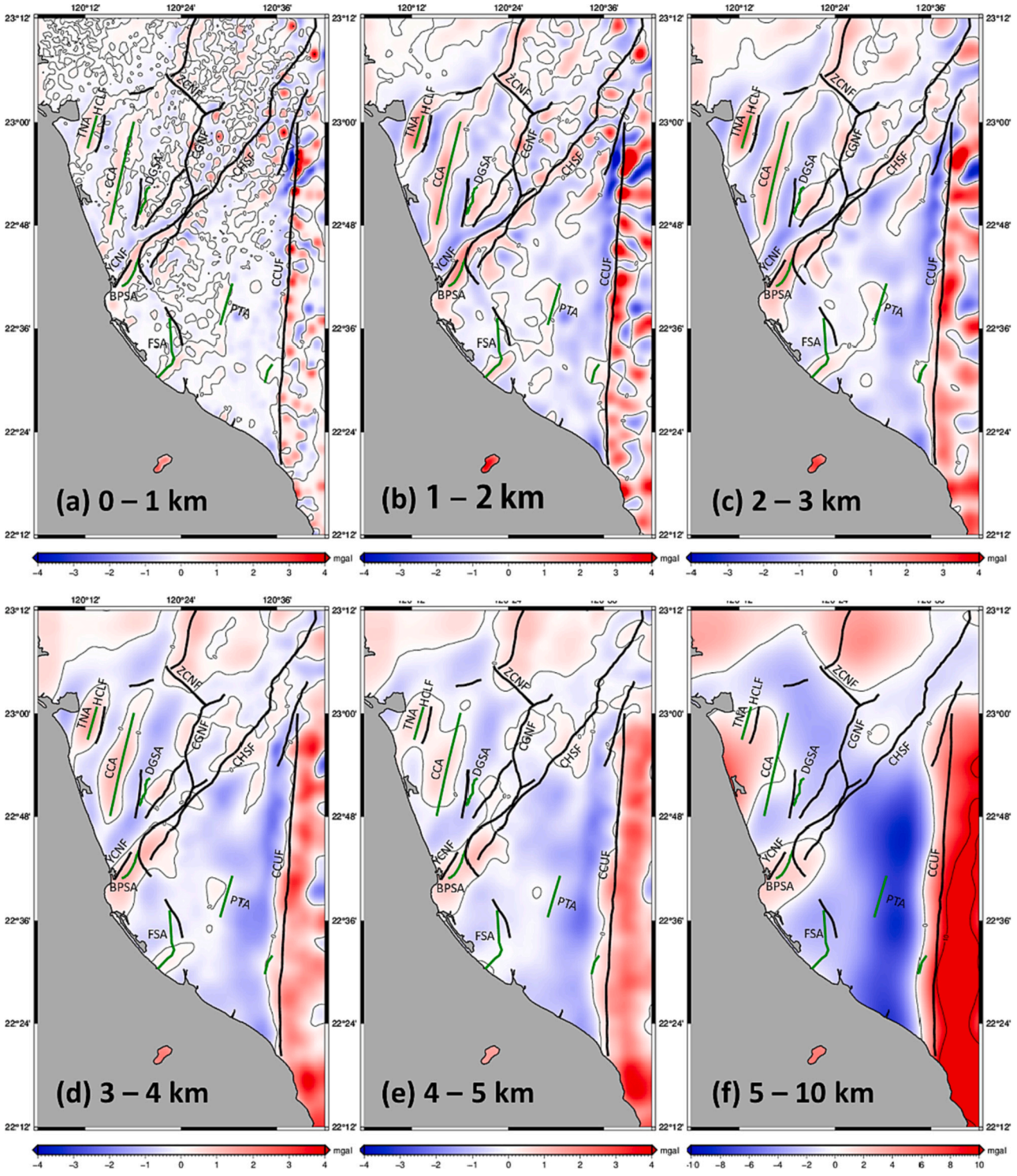

Fig. 5. The residual gravity anomalies corresponding to depth intervals of 1 km from 0 to 5 km and for the depth interval 5–10 km.

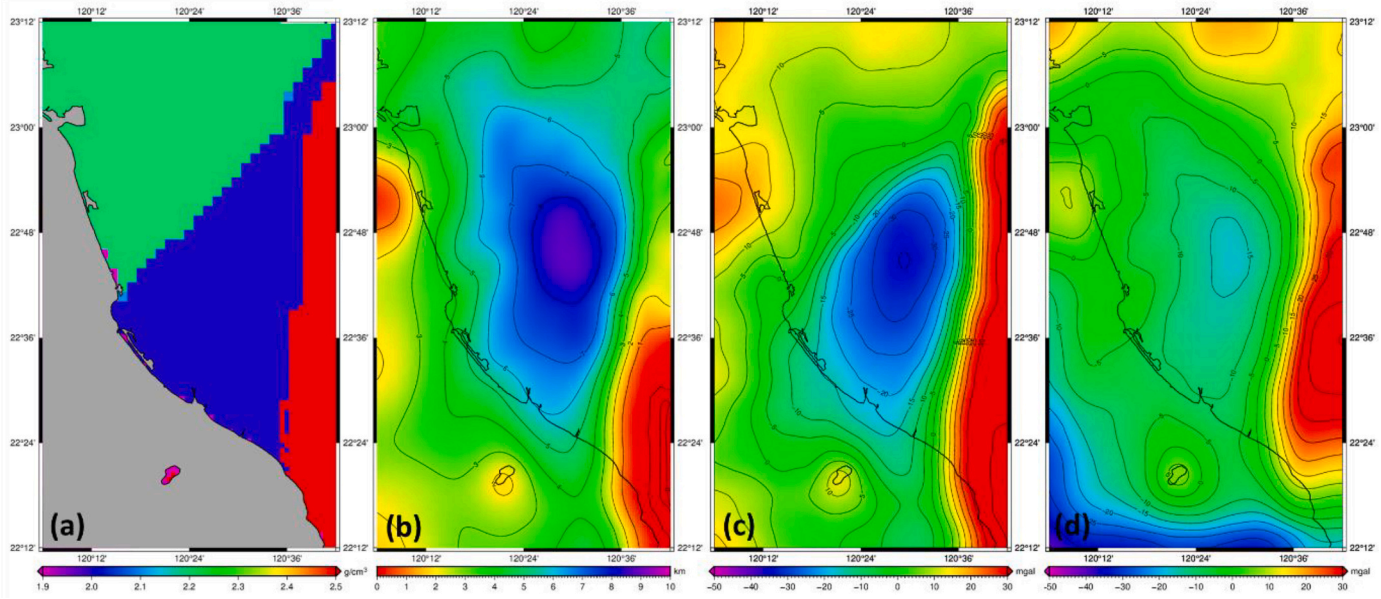

Fig. 6. Initial model showing (a) the near-surface density distribution (0 km depth), (b) basement depth, (c) the calculated forward gravity of initial model, and (d) the calculated forward gravity of initial model assuming a uniform density of the surface rock on each side of the CHSF.

To construct the a priori density model, the three-dimensional seismic tomography is commonly adopted from previous studies based on the relationship between seismic velocity and density (Nafe and Drake, 1957; Ludwig et al., 1970; Barton, 1986; Brocher, 2005; Yen and Hsieh, 2010; Hsieh and Yen, 2016; Tadiello and Braitenberg, 2021; Lo et al., 2018, 2021); however, the observed gravities and the seismic tomography-derived calculated gravities in SW Taiwan are significantly different (Yen and Hsieh, 2010; Lo et al., 2018, 2021). In order to avoid controversy over the suitability of the selected velocity model, we adopted three simple assumptions to construct the initial model based on a large density contrast across the CHSF and the variation of Late Miocene basement depth. These were as follows:

1. A large difference is shown in the rock compositions on each side of the CHSF. The density of strata in southwestern Taiwan (Table 1) was established based on the geological sections and drilling data (Hsieh, 1970). With the CHSF as the boundary, the general densities of the western and eastern layers were 2.2 g/cm^3 and 2.0 g/cm^3; these correspond to the Gtk and the conglomerate layer, respectively (Fig. 6a). If the density contrast across the CHSF is not considered and a uniform density is adopted, the negative anomaly beneath the PTP cannot be modeled (Fig. 6d).
2. The Late Miocene basement depth in our a priori model referred to the results of Lin and Watts (2002) and Yu and Tsai (1981). The greatest depth to basement is approximately 9 km at the center of the Pingtung Plain; the depth is 4 km in the coastal area. If the distribution of gravity anomalies was greatly affected by the thickness of the sedimentary layer, we expressed the relationship between the Bouguer anomaly and the Late Miocene basement depth as follows:

$$H_{base} = H_{shallow} + (BA_i - BA_{shallow})^{*}\left(H_{deep} - H_{shallow}\right)/\left(BA_{deep} - BA_{shallow}\right)$$

While $H_{base} > 0$, then set $H_{base} = 0$where H_{base} is the basement depth, $H_{shallow}$ and H_{deep} are the assumed shallowest and deepest basement depth (set to 4 km and 9 km, respectively); BA_i is the Bouguer anomaly of each point, BA_{deep} and $BA_{shallow}$ are the Bouguer anomalies at basement depths of 4 km and 9 km, (set to −50 mGal and − 10 mGal respectively). The basement depth distribution map is shown in Fig. 6b.

The density model below the Late Miocene basement was set to 2.5 g/cm^3. Compared with other geological models (Camanni et al., 2016; Biete et al., 2018; Brown et al., 2022) that refer to Vp = 5.2 km/s (equivalent to ρ = 2.56 g/cm^3 according to Vp to ρ relationship formula (Brocher, 2005) isovelocity surface as the crystalline basement, the assumption of basement is close to our results.

3. The density of the Lushan Formation was set at 2.55 g/cm^3 east of the CCUF (Fig. 6a).

We set the range of the inverse model such that it extended 20 km in all directions beyond the study area. The modeled depth was set at 10 km with density gradually increasing with depth. The observation points used for inversion were reselected to achieve a uniform distribution in the study area.

4. Results

4.1. Residual gravity anomaly

Residual gravity anomaly maps were calculated for increasing wavelength bands (band pass filters) corresponding to 1-km depth intervals from 0 km to 5 km and the depth interval 5–10 km; the results are shown in Fig. 5, where the maps are labeled according to the depth interval appropriate to the cut off wavelength (using Eq. 1). The spatial variation of the residual anomaly at wavelengths corresponding to a depth of 0–1 km is localized and the variation is small, indicating that there are few shallow structures with a wavelength of <3 km. The trend of anomalies corresponding to depths below 5 km is relatively gentle. The entire PTP is dominated by negative gravity.

The obvious broad gravity lows in the original Bouguer map and the regional gravity anomaly map (Figs. 2b and 4a) have wavelengths of over 30 km, which suggests that the source is theoretically below 10 km depth according to the wavelength filtering method (Jung, 1961). The three-dimensional seismic velocity model of the area (Kuo-Chen et al., 2012; Huang et al., 2014) shows no obvious low-velocity layer below a depth of 10 km. We therefore assumed that the broad low gravity anomalies in the PTP result from a relatively shallow source, and that the basement depth is not >10 km (Lin and Watts, 2002; Yu and Tsai, 1981). Therefore, the wavelength filtering analysis also needs to be

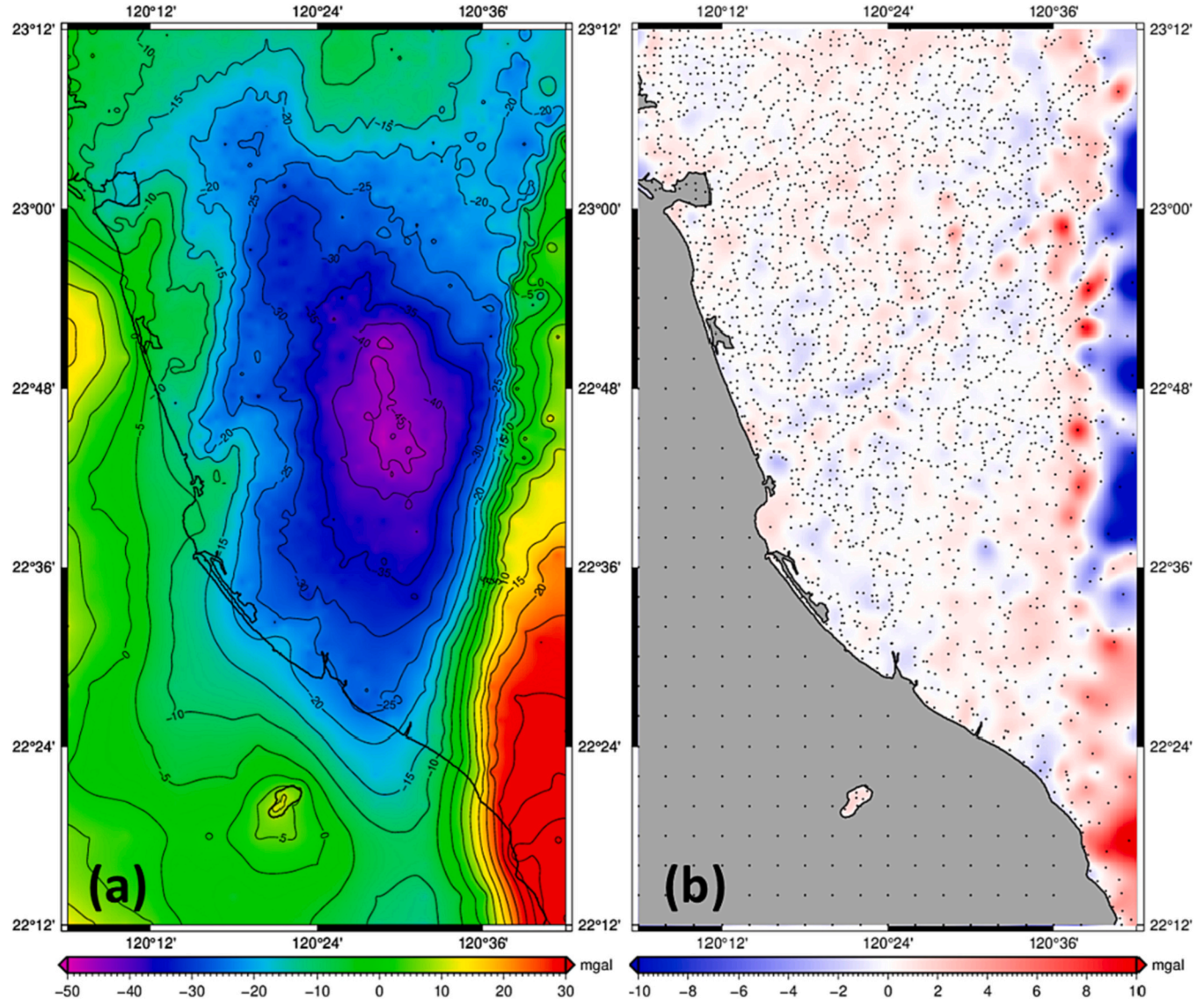

Fig. 7. (a) The calculated gravity values of the inverse model. (b) The difference between the observed gravity values and the calculated gravity values from inversion.

combined with 3D density inversion to recover the 3D subsurface structures.

4.2. 3D forward calculation and the inverse method of density modeling

The settings of our a priori model was reasonable because the difference between the lowest and highest forward gravity values (Fig. 6c) was consistent with the range of observed gravity. The calculated values of the inverted density model are shown in Fig. 7a, with residuals being distributed from −5 mGal to 5 mGal (Fig. 7b). The results of the inverted density model at depths of 0 km to 4 km are shown in Fig. 8 because the density change caused by the gravity inversion is mainly in the range of 0–4 km depth. The distribution of the low-density materials (Fig. 8a-8c) and the basin center location of the PTP (Fig. 8d) were derived from the results of our three-dimensional density inversion. The basement depth of the PTP is also inferred to be approximately 4 to 9 km (profiles BB' and CC' in Fig. 9) if a density of 2.4 to 2.5 g/cm^3 indicates the presence of Late Miocene basement. The deepest basement depth of the PTP is about 9 km in Ligang, which is roughly in the center of the PTP, and it gradually reduces outward to approximately 4 km (Fig. 8).

5. Discussion

The dense gravity network provided good constraints for detecting the lateral density changes of geological structures through wavelength filtering and density inversion. The residual gravity anomalies at different wavelengths clearly reveal the spatial variation of linear structures with depth, which can be inferred by the relationship between the wavelength of the filter and depth.

5.1. Active structures characterized by gravity observations

Although a series of NNE-striking *en echelon* anticlines, e.g., the TNA and CCA, have been detected at the coastal plain in SW Taiwan (Fig. 5) according to the seismic surveys and positive gravity anomalies (Pan, 1968; Hsieh, 1970), the underground shapes of these major anticlines were further characterized in terms of the distribution of positive residual gravity anomalies and relatively high densities in this study (Figs. 11 and 12). The width of residual positive gravity anomaly on the TNA is 5 km, and the positive anomaly dips westward with depth, which is consistent with the distribution of surface topography (Chen et al., 2020). The CCA is also located in the positive gravity anomaly region,

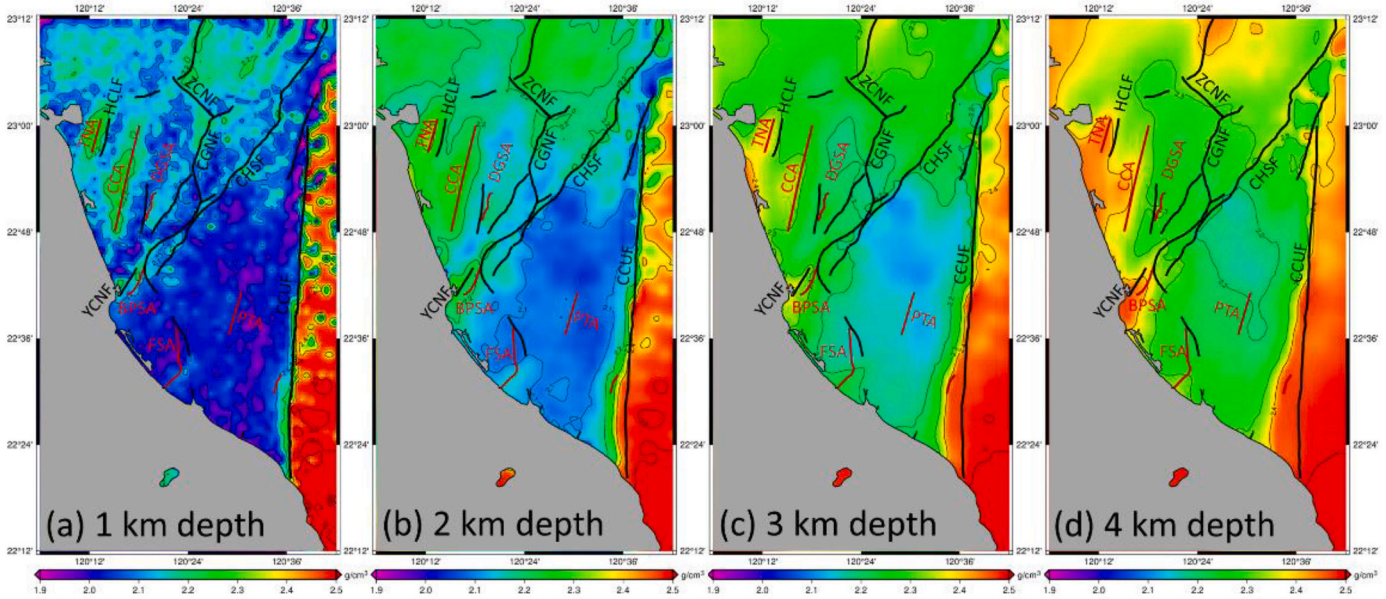

Fig. 8. (a)-(d) Density models after inversion from depths of 1 km to 4 km.

and its positive anomaly is vertically upward with depth. The TNA and CCA have been proposed as mud diapir within the lower Gtk due to detachment folding under compressional stress (Sun, 1964; Pan, 1968; Hsieh, 1972). Compared with the other two sections, the CCA in the B-B′ section (Fig. 11) has a higher gravity anomaly, indicating that the middle section of the CCA has higher density could be caused by higher activity mud diapir uplifting.

Beside the school of mud diapir, the generation of CCA is also suggested as being a west-dipping buried backthrust based on a geological inference (Le Béon et al., 2017; Huang et al., 2004). The Houchiali fault (HCLF) which is also the proposed seismogenic backthrust (Fruneau et al., 2001; Le Béon et al., 2017) lies between a large positive and negative residual gravity anomaly to the east of the TNA. The positive anomaly dips westward with depth in the west of the HCLF (A-A' section, Fig. 11). However, no clear geological evidence is related to these backthrust (Le Béon et al., 2017; Huang et al., 2004). Anomaly comparison pattern of horizontal and vertical velocities is shown in SW Taiwan to indicate the possible presence of mud diapirism (Ching et al., 2016). Therefore, the uplift of mud diapir is still highly possible in SW Taiwan.

Brown et al. (2022) interpreted the fold-and-thrust belt as a west-verging, imbricate thrust system developed above a single basal thrust. The depth of basal thrust varies roughly from 1 to 10 km from west to east in SW Taiwan. It is consistent with the 2.4 g/cm^3 isodensity contour (Fig. 9), and this isodensity contour acts as the basement gradually deepening from west to east. At greater equivalent depths (1–5 km) (Figs. 5b to 5e), several faults are located at the junction of positive and negative anomalies, and the anticline axes coincide with the centerline of the elongated positive anomalies. In addition, the trace of the Chegualin fault (CGNF) is not consistent with the distribution of residual gravity. Because no outcrops of the CGNF and CHSF near the coast have been discovered, we propose that the CGNF may extend southwestward and connect with the Youchang fault (YCNF) based on our gravity analysis.

The Zuochen fault (ZCNF) has been inferred mainly from (1) the presence of linear features in photographs and the drainage pattern (Wang, 1976; Deffontaines et al., 1994, 1997) and (2) the different stratigraphic characteristics on each side of it (Lin et al., 2007). The ZCNF can be identified on the northwestern segment from the terrain alignment, distribution of rock formations, structural types and field outcrops (Lin et al., 2007). The residual gravity anomaly map (Fig. 5) shows noticeably that the east side of the ZCNF is a positive gravity anomaly area, anomalous up to at least 10 km depth, whereas the west side is a negative gravity anomaly area. This indicates that the dip angle of the ZCNF is close to vertical, and there are obvious different stratigraphic characteristics on both sides of the fault extending to the deeper. A large dip angle above 10 km in depth and a dip angle of 41° below 10 km in depth have been suggested for the ZCNF based on the coseismic source model of the 2010 Jiashian earthquake (Ching et al., 2011b).

5.2. Origin of positive residual gravity anomalies

The horizontal distribution of residual gravity and density corresponds well with linear geological structures (Figs. 5 and 9). The positive residual gravity anomaly stripes correspond to anticlines, such as the TNA, CCA, FSA, and BPSA, whereas the negative anomalies correspond to the synclines (Fig. 5). In the vertical sections (Fig. 9), the derived density at the anticlines is slightly higher than the surrounding rocks (by 0.1–0.2 g/cm^3), which is similar to the modeled density results for offshore mud diapirs (Doo et al., 2015). In general, it's hard to directly distinguish mud diapirs or fault-related folds with high-density formation distribution from the residual gravity anomaly map, and shallow geological surveys or drilling results are needed to assist.

Geological drilling data indicate that the TNA and CCA were likely to have been invaded by mud diapirs (Hsieh, 1972). Mud diapirs theoretically become lighter during upward migration because of methane expansion and degassing of a closed system, thus but negative anomalies along anticlines are expected based on the theory of mud diapirs (Brown, 1990). However, mud volcanoes and cracks, which form simultaneously with mud diapirs, could provide a dewatering mechanism that drains off some of the fluid (Breen et al., 1988). In other words, the density of a mud diapir would gradually decrease from depth to the surface due to methane expansion (Fig. 9); however, the dewatered mudstone may be gradually enriched in solid components, which causes the overall density in the diapir to become higher than the surrounding mudstone (Fig. 9). Dewatered mudstones with a density about 2.6 g/cm^3 have been detected by Ku and Hsu (2009) and Chen et al. (2020). According to the results of 44 hydrological drilling (Chen et al., 2020) and CPC deep drilling on the coastal plain, we can obtain the distribution of hard mudstones, which corresponds to the positive residual gravity anomaly (Hsieh, 1972) (Fig. 10). In addition, the positive residual gravity anomaly can also be related to the proposed offshore mud diapirs

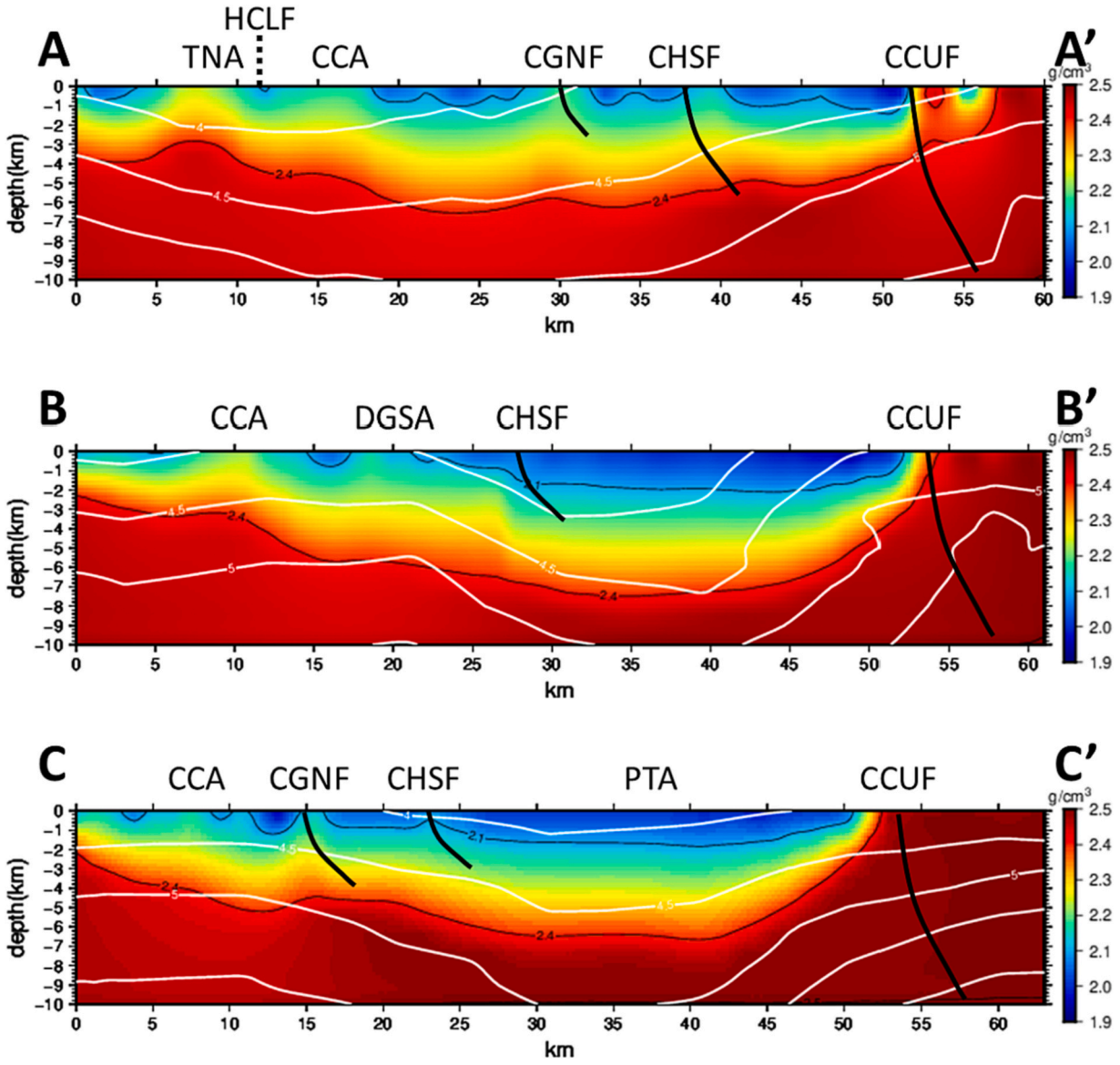

Fig. 9. Three vertical sections showing the variation of density with depth modeled by gravity inversion. The white line shows the contour distribution trend of the P-wave velocity model (Huang et al., 2014).

in SW Taiwan (Sun and Liu, 1993; Sibuet and Hsu, 2004; Ku and Hsu, 2009; Doo et al., 2015). Mud diapirs have been proposed as one of mechanism in the formation of the anticlines in southwestern Taiwan (e.g., Hsieh, 1972; Chen and Liu, 2000; Chen et al., 2014, 2020).

Based on the sections of the residual gravity anomalies (Fig. 11), the positive residual gravity anomaly of the TNA disappears at a depth of 4–5 km. The anomaly of the CCA disappears at a depth of approximately 4 km in section AA', and disappears at a depth of 3–4 km in sections BB' and CC'. The positive gravity associated with the CGNF also extends to 4 km, and the positive gravity below the CHSF extends to approximately 6 km in sections AA' and CC'. In terms of the derived bottom depth of the Gtk from the analysis of the geological balanced cross sections, the proposed bottom of the mud diapirs is approximately 5 km (Huang et al., 2004; Le Béon et al., 2017). After verification by model testing of wavelength filtering method, we explain that the mud diapirs with positive gravity anomaly were generated from the Gtk at approximately 4–5 km in depth and then arched to produce anticlines.

On the other hand, we can also use the concept of thrust faults (Biete et al., 2018; Brown et al., 2022) and backthrust faults (Le Béon et al., 2017) to explain the occurrence of positive anomalies. Thrust and backthrust faults cause the relatively high density of Gtk to bulge the surface, forming a fault-related fold and causing the surface gravity observation to show a positive anomaly. In addition, the positive anomalies in the hanging wall of the CHSF are most likely related to the compacted sandstone.

According to the geodetic data inversion using the dislocation fault model (Ching et al., 2016), the active faults and mud diapirs are two possible mechanisms dominating the active anticlines in SW Taiwan. However, the structure of high-density mudstone beneath the SW Taiwan are still debated. We believe that the origin of positive residual gravity anomalies can be roughly divided into three types (Fig. 12) corresponding to the possible subsurface structures.

Type 1: Over the west side of the study area, including the TNA and CCA, the high positive gravity anomalies are caused by the intrusion of high-density mudstone. The high-density mudstone has been demonstrated from drilling data and can be connected with offshore mud diapirs.

Type 2: The positive anomaly area near the CGNF is the mudstone-fault dominated transition zone. The positive gravity anomaly value lower than the TNA and CCA regions may be due to amounts of water

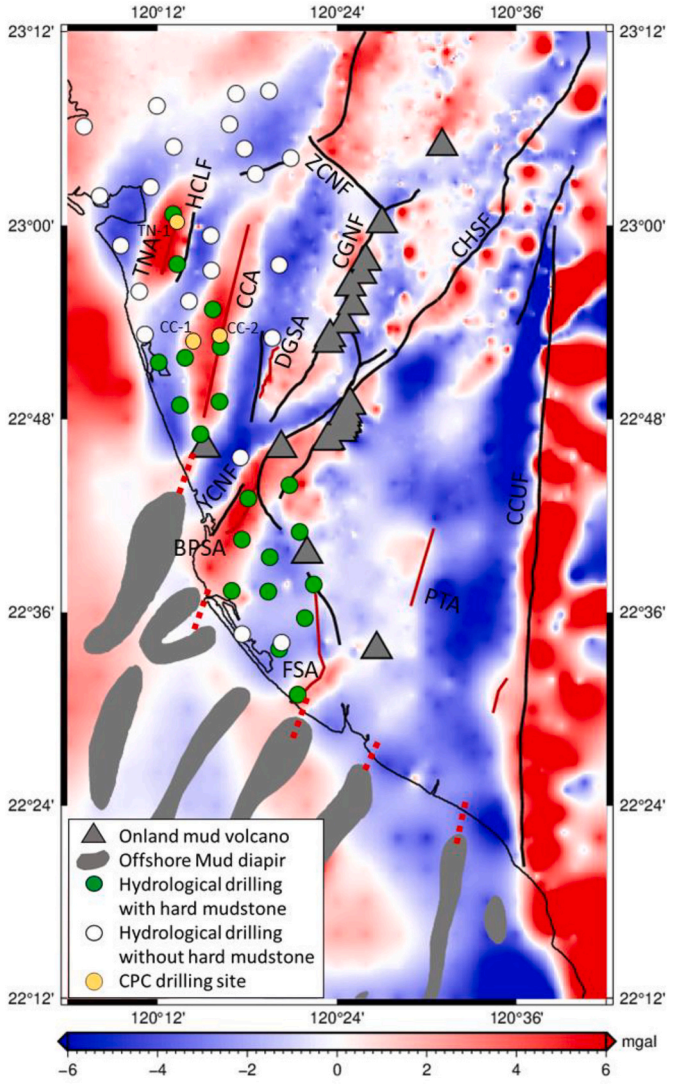

Fig. 10. The distribution of mud volcanoes onshore and mud diapirs offshore superimposed on the 0–5 km residual gravity anomaly map.

and gas mudstone in the shallower or the mud volcano eruption in the deeper. And CGNF can be regarded as the channel of eruption.

Type 3: The positive anomaly along the CHSF mainly distributes on the hanging wall and the negative gravity anomalies are shown on the footwall of fault. Therefore, the positive gravity anomaly should be related to the exhumation of high-density formation along the thrust.

5.3. Gravity low in the Pingtung Plain

A broad distribution of low-gravity anomalies in the PTP is thought to be caused by a deep sedimentary trough (Pan, 1968; Hsieh, 1970; Yu and Tsai, 1981). This depth range is generally comparable to the inferred depth of the magnetic basement of 8–9 km (Yu and Tsai, 1981). Our inferred basement depth is also comparable to the results of the contour distribution trend of the P-wave velocity model (Huang et al., 2014). A velocity discontinuity at 10 km in depth below the PTP was also derived from receiver function studies (Tang et al., 2011).

The C-C′ section in Fig. 9 is a section across the PTP, and its structural characteristics are similar to Chiang (1971) combines seismic reflection, drilling, and gravity data to discuss the structural characteristic of the PTP. According to our forward and inversion results, the low gravity in the PTP results from (1) the high-density contrasts on both sides of the CHSF and the CCUF and (2) the deepening of the PTP basement. The relatively high-density materials west of the CHSF comprise the Gtk with a series of anticlines and faults (Huang et al., 2004). On the contrary, the shallow material of the PTP to the east of the CHSF is dominated by a conglomerate layer of relatively low density (Sun, 1965). The CCUF is a high-angle thrust fault along the east of the PTP with the highest gravity gradient (Fig. 2b), which was also identified by the receiver function study (Tang et al., 2011). The relatively high gravity anomaly is exposed on the east side of the CCUF as the high-density Miocene Lushan Formation. In addition, the minor positive gravity anomalies are distributed along the PTA and range from 1 km to 4 km depth (Fig. 5), indicating that the PTA is arched at depth in the PTP but there is no surface exposure. This result is consistent with the geological profile obtained with drilling control (Cheng, 2000).

In summary, (1) the geometries of diapiric anticlines and active faults can be characterized by a dense gravity survey; (2) the nearly vertical ZCNF above 10 km in depth is proposed in terms of the obvious gravity anomaly boundary; (3) the bottom depth of the mud diapirs in southwestern Taiwan is approximately 4–5 km; and (4) the active faults and mud diapirs are only two of the possible mechanisms dominating the active anticlines in SW Taiwan. Finally, we propose a three-dimensional conceptual model based on the Bouguer gravity anomaly (Fig. 13) to summarize the subsurface structures in southwestern Taiwan. The variation of the shallow gravity anomaly is mainly affected by the fault and fold system, and the variation of the deep gravity anomaly is dominated by the change of the basement depth.

6. Conclusions

An accurate Bouguer gravity anomaly map obtained through dense gravity surveys resolves subsurface structures at different depths using the wavelength filtering analysis method. Regarding the geometries of the active faults in SW Taiwan, the location of the fault line can be defined by the boundary of positive and negative residual anomalies. The CGNF, identified by the residual gravity map in this study, should extend southwestward to the YCNF and continue offshore. The nearly vertical ZCNF above 10 km in depth, is identified in terms of an obvious gravity anomaly boundary. It should be noted that several active anticlines are located on the axis of the positive residual anomaly.

The positive residual gravity anomaly is presumed to be related to the anticline structure and the higher-density material that is produced by mudstone dewatering and/or fault-related fold. Active faults, high-density mudstone, and mud volcanoes are exposed in shallow layers in SW Taiwan. According to the cause of gravity anomaly, it can be roughly divided into three types: (1) caused by the intrusion of high-density mudstone in the TNA and CCA fold areas. The presence of high-density mudstone in southwestern Taiwan was proposed along active anticlines, such as the TNA and CCA, in this study based on the distributions of the positive residual gravity anomalies, mud volcanoes, and hard mudstone identified by drilling. The depth of the cause of the positive gravity anomaly of the TNA and CCA is 4–5 km, corresponding to the bottom of the Gtk. The density of the anticline was 0.1–0.2 g/cm^3 higher than the surrounding rock and the residual gravity value was slightly higher by 1–2 mGal; (2) The positive anomaly area near the CGNF is the mudstone-fault dominated transition zone. The positive gravity anomaly value lower than the TNA and CCA regions may be due to amounts of water and gas mudstone in the shallower or the mud volcano eruption in the deeper. And CGNF can be regarded as the channel of eruption; (3) The positive anomaly near the CHSF is dominated by the fault thrust of the high-density formation to the surface, the positive gravity anomaly should be related to the exhumation of high-density formation along the thrust.

We used three-dimensional density inversion to assist in the analysis of the tectonic features in the shallow part of the PTP. We constructed an initial density model that is based on the density contrast on either side of the CHSF and CCUF and the variation of the basement depth. According to our forward and inversion results, the low gravity in the PTP

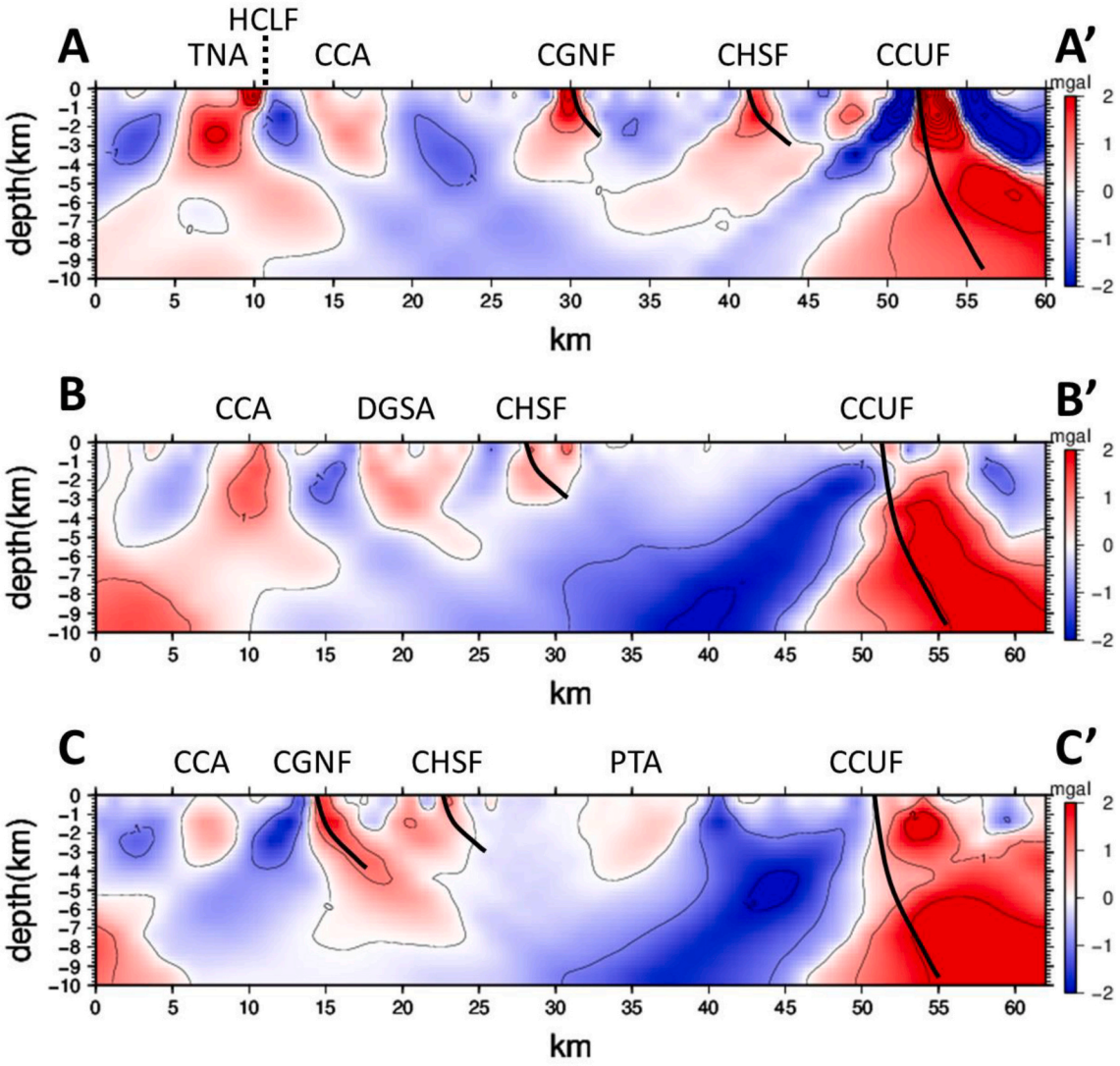

Fig. 11. Three sections of residual gravity anomaly variation with depth.

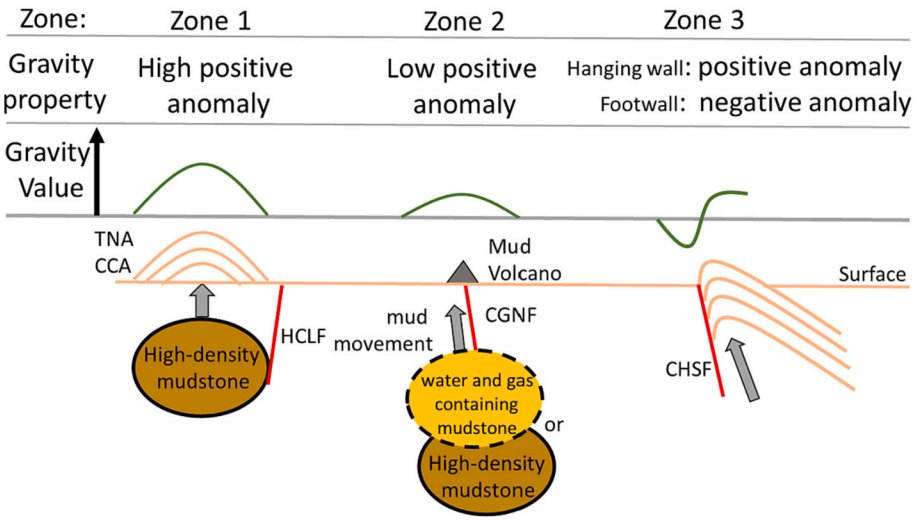

Fig. 12. Schematic diagram of origin of positive residual gravity anomalies zones.

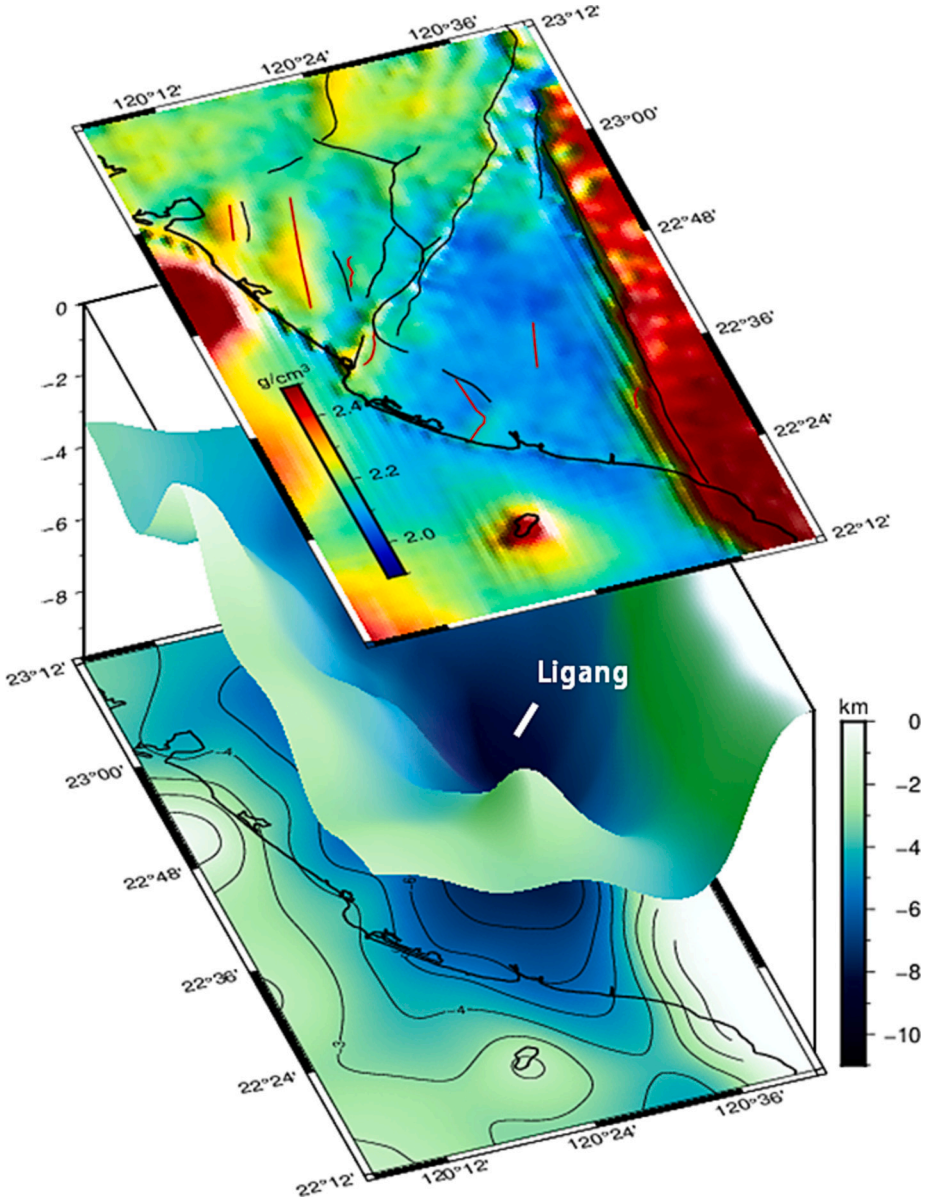

Fig. 13. Conceptual image of 3D subsurface structures in SW Taiwan.

results from (1) the high-density contrasts on both sides of the CHSF and the CCUF and (2) the deepening of the PTP basement. Through wavelength filtering analysis and three-dimensional density inversion, we also concluded that the CCUF is a high-angle thrust fault at shallow depths and that the basement depth gradually deepens from the west side of the CCUF to the center of the PTP.

Acknowledgement

We are grateful to the Editor and two reviewers for their constructive comments on the manuscript. Figures were generated using the Generic Mapping Tools (GMT).

CRediT authorship contribution statement

Yu-Tsung Lo: Conceptualization, Methodology, Software, Validation, Formal analysis, Data curation, Writing – original draft. **Kuo-En Ching:** Validation, Investigation, Writing – review & editing. **Horng-Yuan Yen:** Formal analysis, Writing – review & editing, Funding acquisition. **Song-Chuen Chen:** Validation, Investigation, Visualization.

Declaration of Competing Interest

The authors declare that they have no known competing financial interests or personal relationships that could have appeared to influence the work reported in this paper.

Data availability

Data will be made available on request.

References

Barton, P.J., 1986. The relationship between seismic velocity and density in the continental crust - a useful constraint? Geophys. J. R. Astron. Soc. 87, 195–208.

Biete, C., Alvarez-Marron, J., Brown, D., Kuo-Chen, H., 2018. The structure of southwest Taiwan: the development of a fold-and-thrust belt on a margins outer shelf and slope. Tectonics 37, 1973–1993. https://doi.org/10.1029/2017TC004910.

Breen, N.A., Tagudin, J.E., Reed, D.L., Silver, E.A., 1988. Mud-cored parallel folds and possible melange development in the north Panama thrust belt. Geology 16, 207–210.

Brocher, T.M., 2005. Empirical relations between elastic wave speeds and density in the Earth's crust. Bull. Seismol. Soc. Am. 95, 2081–2092. https://doi.org/10.1785/0120050077.
Brown, K.M., 1990. The nature and hydrogeologic significance of mud diapirs and diatremes for accretionary systems. J. Geophys. Res. 95, 8969–8982.
Brown, D., Alvarez-Marron, J., Camanni, G., Biete, C., Kuo-Chen, H., Wu, Y.M., 2022. Structure of the south-central Taiwan fold-and-thrust belt: testing the viability of the model. Earth Sci. Rev. 231, 104094.
Camanni, G., Alvarez-Marron, J., Brown, D., Ayala, C., Wu, Y.-M., Hsieh, H.-H., 2016. The deep structure of south-central Taiwan illuminated by seismic tomography and earthquake hypocentre data. Tectonophysics 679, 235–245.
Chang, S.L., Yuan, J., Hsiao, P.T., Chi, W.R., 1982. The neogene series, tectonic evolution, and petroleum potentialities of Southwestern Taiwan. In: Transactions of the 3rd Circum-Pacific Energy and Mineral Resources Conference, pp. 577–587.
Chang, C.P., Angelier, J., Lee, T.Q., Huang, C.Y., 2002. From continental margin extension to collision orogen: structural development of the Hengchun Peninsula and tectonic rotation, southern Taiwan. Tectonophysics 361, 61–82.
Chang, C.P., Angelier, J., Lu, C.Y., 2009. Polyphase deformation in a newly emerged accretionary prism: folding, faulting and rotation in the southern Taiwan mountain range. Tectonophysics 466, 395–408. https://doi.org/10.1016/j. tecto.2007.11.002.
Chen, Y.G., Liu, T.K., 2000. Holocene uplift and subsidence along an active tectonic margin southwestern Taiwan. Quat. Sci. Rev. 19, 923–930.
Chen, S.C., Hsu, S.K., Wang, Y., Chung, S.H., Chen, P.C., Tsai, C.H., Liu, C.S., Lin, H.S., Lee, Y.W., 2014. Distribution and characters of the mud diapirs and mud volcanoes off southwest Taiwan. J. Asian Earth Sci. 92, 201–214.
Chen, S.C., Ching, K.E., Lo, Y.T., Lu, W.C., 2020. Mud diapiric characters, activities and geohazards of the Tainan and Chungchou anticlines. Bull. Central Geol. Survey, MOEA 33, 1–32 (in Chinese).
Cheng, H.C., 2000. Structural geology of the Tainan to Pingtung area of southwestern Taiwan. MSc thesis,. National Central University, Taiwan, p. 92.
Chiang, 1971. Seismic study of The Chaochou structure, Pingtung, Taiwan. Petrol. Geol. Taiwan No.8, 281–294.
Ching, K.E., Rau, R.J., Lee, J.C., Hu, J.C., 2007. Contemporary deformation of tectonic escape in SW Taiwan from GPS observations, 1995-2005. Earth Planet. Sci. Lett. 262, 601–619.
Ching, K.E., Hsieh, M.L., Johnson, K.M., Chen, K.H., Rau, R.J., Yang, M., 2011a. Modern vertical deformation rates and mountain building in Taiwan from precise leveling and continuous GPS observations, 2000–2008. J. Geophys. Res. 116, B08406. https://doi.org/10.1029/2011JB008242.
Ching, K.E., Johnson, K.M., Rau, R.J., Chuang, R.Y., Kuo, L.C., Leu, P.L., 2011b. Inferred fault geometry and slip distribution of the 2010 Jiashian, Taiwan, earthquake is consistent with a thick-skinned deformation model. Earth Planet. Sci. Lett. 301, 78–86.
Ching, K.E., Gourley, J.R., Lee, Y.H., Hsu, S.C., Chen, K.H., Chen, C.L., 2016. Rapid deformation rates due to development of diapiric anticline in southwestern Taiwan from geodetic observations. Tectonophysics 692, 241–251. ISSN 0040-1951,. https://doi.org/10.1016/j.tecto.2015.07.020.
Chou, J.T., 1971. A preliminary study of the stratigraphy and sedimentation of the mudstone formations in the Tainan area, southern Taiwan. Petrol. Geol. Taiwan 8, 87–219.
Deffontaines, B., Lee, J.C., Angelier, J., Carvalho, J., Rudant, J.P., 1994. New geomorphic data on the active Taiwan orogen: a multisource approach. J. Geophys. Res. 99, 20,243–20,266.
Deffontaines, B., Lacombe, O., Angelier, J., Chu, H.T., Mouthereau, F., Lee, C.T., Deramond, J., Lee, J.F., Yu, M.S., Liew, P.M., 1997. Quaternary transfer faulting in the Taiwan Foothills: evidence from a multisource approach. Tectonophysics 274, 61–82.
Doo, W.B., Hsu, S.K., Lo, C.L., Chen, S.C., Tsai, C.H., Lin, J.Y., Huang, Y.P., Huang, Y.S., Chiu, S.D., Ma, Y.F., 2015. Gravity anomalies of the active mud diapirs off southwest Taiwan. Geophys. J. Int. Geophy. Suppl. Monthly Notices Royal Astronom. Soc. 203, 2089–2098. https://doi.org/10.1093/gji/ggv430.
Fruneau, B., Pathier, E., Raymond, D., Deffontaines, B., Lee, C.T., Wang, H.T., Angelier, J., Rudant, J.P., Chang, C.P., 2001. Uplift of Tainan Tableland (SW Taiwan) revealed by SAR interferometry. Geophys. Res. Lett. 28, 3071–3074. https://doi.org/10.1029/2000GL012437.
Ho, C.S., 1986. An Introduction to the Geology of Taiwan: Explanatory Text of the Geologic Map of Taiwan. Central Geological Survey, MOEA, Taipei, ROC, p. 163 (in Chinese).
Hsieh, S.H., 1970. Geeology and gravity anomalies of the Pingtung Plain, Taiwan. In: Proceedings of the Geological Society of China, 13, pp. 76–89.
Hsieh, S.H., 1972. Subsurface geology and gravity anomalies of the Tainan and Chungchou structures of the coastal plain of southwestern Taiwan. Petrol. Geol. Taiwan 10, 323–338.
Hsieh, H.H., Yen, H.Y., 2016. Three-dimensional density structures of Taiwan and tectonic implications based on the analysis of gravity data. J. Asia Earth Sci. 124, 247–259.
Huang, S.T., Yang, K.M., Hung, J.H., Wu, J.C., Ting, H.H., Mei, W.W., Hsu, S.H., Lee, M., 2004. Deformation front development at the northeast margin of the Tainan basin, Tainan-Kaohsiung area, Taiwan. Mar. Geophys. Res. 25, 139–156. https://doi.org/10.1007/s11001-005-0739-z.
Huang, H.H., Wu, Y.M., Song, X.D., Chang, C.H., Lee, S.J., Chang, T.M., Hsieh, H.H., 2014. Joint Vp and Vs tomography of Taiwan: Implications for subduction-collision-orogeny. Earth Planet. Sci. Lett. 392, 177–191. https://doi.org/10.1016/j.epsl.2014.02.026.
Jung, K., 1961. Schwerkraftverfahren in der angewandten Geophysik. Akademische Verlagsgesellschaft Geest & Portig, Leipzig, p. 348.
Ku, C.Y., Hsu, S.K., 2009. Crustal structure and deformation at the northern Manila Trench between Taiwan and Luzon Islands. Tectonophysics 466, 229–240.
Kuo-Chen, H., Wu, F.T., Roecker, S.W., 2012. Three-dimensional P velocity structures of the lithosphere beneath Taiwan from the analysis of TAIGER and related seismic datasets. J. Geophys. Res. Solid Earth 117, B06306. https://doi.org/10.1029/2011JB009108.
Le Béon, M., Huang, M.H., Suppe, J., Huang, S.T., Pathier, E., Huang, W.J., Chen, C.L., Fruneau, B., Baize, S., Ching, K.E., Hu, J.C., 2017. Shallow geological structures triggered during the Mw 6.4 Meinong earthquake, southwestern Taiwan. Terr. Atmos. Ocean. Sci. 28, 663–681.
Lin, A.T., Watts, A.B., 2002. Origin of the West Taiwan basin by orogenic loading and flexure of a rifted continental margin. J. Geophys. Res. Solid Earth 107, 2185. https://doi.org/10.1029/2001JB000669.
Lin, C.W., Lu, S.T., Shih, T.S., Liu, Y.C., Lin, W.H., Lin, Y.H., 2007. Active Faults of Southwestern Taiwan: Explanatory Text for the Strip Maps of Active Faults Scale 1: 25,000, 17. Special Publication of the Central Geological Survey, p. 141.
Lo, Y.T., Yen, H.Y., Chen, C.R., 2018. Correlation between the Bouguer gravity anomaly and the TAIGER tomography of the Taiwan region. Terr. Atmos. Ocean. Sci. 29, 473–483. https://doi.org/10.3319/TAO.2018.03.01.01.
Lo, Y.T., Huang, H.H., Yen, H.Y., 2021. Probing depth origin of gravity anomalies in Taiwan through 3-D coherent velocity model. Terr. Atmos. Ocean. Sci. 32, 305–317. https://doi.org/10.3319/TAO.2021.04.30.01.
Ludwig, W.J., Nafe, J.E., Drake, C.L., 1970. Seismic refraction. In: Maxwell, A.E. (Ed.), The Sea, 4. Wiley-Interscience, NewYork, pp. 53–84.
Mouthereau, F., Deffontaines, B., Lacombe, O., Angelier, J., 2002. Variation along the strike of the Taiwan thrust belt: basement control on structural style, wedge geometry, and kinematics. Geol. Soc. Am. Spec. Pap. 358, 31–54.
Nafe, J.E., Drake, C.L., 1957. Variation with depth in shallow and deep water marine sediments of porosity, density and the velocities of compressional and shear waves. Geophysics 22, 523–552.
Pan, Y.S., 1968. Interpretation and seismic coordination of the bouguer gravity anomalies obtained in southwestern Taiwan. Petrol. Geol. Taiwan 6, 197–208.
Rau, R.-J., Wen, Y.Y., Ching, K.-E., Hsieh, M.C., Lo, Y.T., Chiu, C.Y., Hashimoto, M., 2022. Origin of coseismic anelastic deformation during the 2016 Mw 6.4 Meinong Earthquake, Taiwan. Tectonophysics 836, 229428. https://doi.org/10.1016/j.tecto.2022.229428.
Shyu, J.B.H., Sieh, K., Chen, Y.G., Liu, C.-S., 2005. Neotectonic architecture of Taiwan and its implications for future large earthquakes. J. Geophys. Res. Solid Earth 110 (8), 1–33. B08402.
Sibuet, J.C., Hsu, S.K., 2004. How was Taiwan created? Tectonophysics 379, 159–181.
Sun, S.C., 1964. Photogeologic study of the Tainan-Kaohsiung coastal plain area, Taiwan. Petrol. Geol. Taiwan 3, 39–51.
Sun, S.C., 1965. On the occurrence of an unconformity in the upper Miocene Wushan Formation and Kaitzuliao Shale near Shegshui-tsun, Kaohsiung, Taiwan. In: Proceedings of the Geological Society of China, 8, pp. 100–101.
Sun, S.C., Liu, C.S., 1993. Mud diapir and submarine channel deposits in offshore Kaohsiung-Hengchun, southwest Taiwan. Petrol. Geol. Taiwan 28, 1–14.
Suppe, J., 1981. Mechanics of mountain-building and metamorphism in Taiwan. Memoir Geol. Soc. China 4, 67–89.
Tadiello, Davide, Braitenberg, Carla, 2021. Gravity modeling of the Alpine lithosphere affected by magmatism based on seismic tomography. Solid Earth. 12, 539–561. https://doi.org/10.5194/se-12-539-2021.
Tang, C.C., Zhu, L., Chen, C.H., Teng, T.L., 2011. Significant crustal structural variation across the Chaochou Fault, southern Taiwan: new tectonic implications for convergent plate boundary. J. Asian Earth Sci. 41, 564–570.
Teng, L.S., 1987. Stratigraphic records of the late Cenozoic Penglai orogeny of Taiwan. Acta Geol. Taiwan. 25, 205–224.
Wang, S., 1976. ERTS-1 satellite imagery and its application in regional geologic study of southwestern Taiwan. Petrol. Geol. Taiwan 13, 37–57.
Yen, H.Y., Hsieh, H.H., 2010. A study on the compatibility of 3-D seismic velocity structures with gravity data of Taiwan. Terr. Atmos. Ocean. Sci. 21, 897–904.
Yen, H.Y., Yeh, Y.H., Lin, C.H., Chen, K.J., Tsai, Y.B., 1995. Gravity survey of Taiwan. J. Phys. Earth 43, 685–696.
Yu, S.B., Tsai, Y.B., 1981. Geomagnetic investigations in the Pingtung plain, Taiwan. Bull. Inst. Earth Sci. Acad. Sin. 1, 189–208.
Yu, S.B., Chen, H.Y., Kuo, L.C., 1997. Velocity field of GPS stations in the Taiwan area. Tectonophysics 274, 41–59.